JGR Oceans

RESEARCH ARTICLE
10.1029/2023JC019858

Key Points:
- Monthly, median nitrate profiles were constructed for five hydrographic zones in the Argentine Basin, defined using θ at 100 m
- Seasonal nitrate drawdown/net community production decreased from 4 to <1 mol C m^{-2} yr^{-1} moving from south to north across the study area
- Chlorophyll data suggest photosynthesis was persistent through austral summer, though most nitrate-based production occurred during spring

Supporting Information:

Supporting Information may be found in the online version of this article.

Correspondence to:

M. B. Alkire,
alkirem@uw.edu

Citation:

Alkire, M. B., & Riser, S. (2023). Net community production in the Argentine Basin estimated from nitrate drawdown using biogeochemical Argo floats. *Journal of Geophysical Research: Oceans*, *128*, e2023JC019858. https://doi.org/10.1029/2023JC019858

Received 22 MAR 2023
Accepted 3 AUG 2023

Author Contributions:

Conceptualization: Matthew B. Alkire
Formal analysis: Matthew B. Alkire
Funding acquisition: Stephen Riser
Methodology: Matthew B. Alkire
Project Administration: Stephen Riser
Software: Matthew B. Alkire
Supervision: Stephen Riser
Writing – original draft: Matthew B. Alkire
Writing – review & editing: Stephen Riser

Net Community Production in the Argentine Basin Estimated From Nitrate Drawdown Using Biogeochemical Argo Floats

Matthew B. Alkire[1] and **Stephen Riser**[1]

[1]University of Washington, Seattle, WA, USA

Abstract

Net community production (NCP) was estimated from nitrate profiles measured via biogeochemical Argo floats drifting in the Argentine Basin. Two criteria were tested for defining hydrographic fronts used to separate the study area into five zones: potential density anomaly at 450 m and potential temperature at 100 m. The latter definition was preferred as it minimized overlapping among zones. Float profiles within each zone were used to construct monthly median profiles of nitrate. Monthly nitrate inventories were calculated for each zone by integrating the median profiles between the surface and a depth of 100 or 200 m. Three methods were utilized to estimate NCP from the nitrate drawdown. The resulting mean NCP estimates indicated a decline in NCP from 3 to 4 mol C m^{-2} yr^{-1} south of ~40°S to ≤1 mol C m^{-2} yr^{-1} north of ~40°S. The monthly median profiles suggested 20%–100% of drawdown occurred by the end of December; however, chlorophyll fluorescence indicated phytoplankton activity persisted through austral summer. We speculate that primary production during these summer months was supported by regenerated nitrogen sources (not nitrate), despite replete concentrations, likely due to the relative scarcity of bioavailable iron known to persist in the region. While a northward advective flux of nitrate was strongly suggested by meridional nitrate gradients over the upper 0–300 m, vertical mixing was apparently necessary to stimulate new production, indicating both processes are important for NCP in the Argentine Basin. This work highlights the potential for floats in studying biogeochemical cycles in hydrographically complex regions.

Plain Language Summary

Robotic floats collect measurements of temperature, salinity, dissolved oxygen, nitrate, and chlorophyll fluorescence across the global ocean. These measurements can be used to estimate the net production of carbon by algae over a specified region, by determining the seasonal reduction in nitrate, an important component of photosynthesis. However, certain areas of the ocean are characterized by numerous fronts, across which temperature, nitrate, and other variables may be very different. It is important to take such fronts into consideration while estimating the nitrate drawdown in such regions. In this study, fronts are identified in the Argentine Basin using potential temperature measurements at 100 m. These fronts were used to divide the Argentine Basin into five zones. Vertical profiles of nitrate were used to construct a single median profile for each zone during each month (January-December). The seasonal changes in these median profiles were used to estimate the production of carbon within each zone. The carbon production was highest in the southernmost zone and decreased moving northward. In addition, most of the nitrate drawdown occurred during austral spring whereas chlorophyll measurements suggested photosynthesis persisted throughout the spring and summer.

1. Introduction

The Argentine Basin is dynamically complex in its hydrography, as it is a region wherein a western boundary current (the Brazil Current) collides with a northward-flowing branch of the Antarctic Circumpolar Current (ACC) after its flow through the Drake Passage (Gordon, 1989; Jullion et al., 2010; Peterson & Whitworth, 1989). The meeting of the cold, relatively fresh and nutrient rich waters from the Southern Ocean with the warm, saline, and nutrient poor waters of the Subtropical Atlantic results in a region of high eddy kinetic energy (Gordon, 1989; Provost et al., 1995). The northward propagation of the nutrient rich waters of the Antarctic, as well as the mesoscale activity in the region, have the potential to foster high rates of export production in the Argentine Basin (Siegel et al., 2014) making it an area of importance for annual carbon dioxide uptake and potential sequestration (Dunne et al., 2007; Schlitzer, 2002).

Argo floats have collected temperature and salinity measurements from the Argentine Basin since 2008, with measurements of nitrate (NO_3^-) available starting in 2016 (Biogeochemical Argo, or BGC-Argo, data reported here were collected between 2016 and 2021). Floats nominally collect vertical profiles every ∼10 days from ∼2,000 db to the surface. The data collected from these floats allow for year-round measurements that are typically not possible with traditional, ship-based methods. Indeed, prior studies have demonstrated the utility of floats for quantifying net community production (NCP) from the time series of data provided by a single float (Plant et al., 2016) as well as a broader estimate of mean NCP over a larger oceanic region (e.g., Johnson et al., 2017b). However, quantifying NCP within the Argentine Basin is especially challenging due to the presence of multiple hydrographic fronts in the region as well as eddies/mesoscale structures. As a result of this complexity, float data cannot be treated as simple timeseries since movement of a single float across a hydrographic front/distinct water mass negates the assumption that spatial variations may be ignored.

A single float is likely to cross one or more of these fronts during its lifetime (Figure 1), and most of the floats used in this study did cross fronts, such that the observation of a full annual cycle by one float without crossing a front was very rare. We have therefore sought to minimize the impact of front crossings by identifying major hydrographic fronts to separate the data into distinct zones that are less horizontally heterogeneous (reduce spatial gradients). Considerations were also made to minimize the potential influences of vertical mixing and entrainment. One such method that might be used to reduce the impact of vertical mixing on NCP calculations employing geochemical budgets involves the assignment of an isopycnal as the bottom boundary of the productive "layer" over which seasonal/monthly/annual changes in nitrate are evaluated (e.g., Alkire et al., 2012). However, attempts to employ isopycnals as bottom boundaries were complicated by the large variability in isopycnal depths across the study region and within each defined zone.

In this study, we endeavor to use BGC-Argo float data to estimate NCP after separating the Argentine Basin into hydrographic zones that reflect the physical and geochemical characteristics of the Southern Ocean, Subtropical Gyre, and varying degrees of mixing between these two regimes.

2. Hydrographic Setting

The general circulation and hydrography of the Argentine Basin is dominated by the interaction of two major currents, the ACC and the Brazil Current (BC). The ACC is organized into three main fronts within the Drake Passage: the Subantarctic Front (SAF), Polar Front (PF), and Southern ACC Front (SACCF); these three fronts extend both eastward and northward into the Argentine Basin from the Drake Passage (Orsi et al., 1995; Peterson & Whitworth, 1989). The SAF turns sharply northward, essentially becoming the Malvinas Current (MC), and transports cold and fresh Antarctic waters along the South American continental slope until these waters collide with the BC that transports relatively warm and salty subtropical waters southward, at ∼40°S (Figure 2). The point of convergence between these two currents, the Brazil Current Front (BCF) or Brazil-Malvinas Confluence (BMC), exhibits eddy kinetic energy that is among the highest in the world ocean (Volkov & Fu, 2008). After colliding, the MC turns sharply back southward while the BC continues to ∼44°S before turning eastward. The center of the Argentine Basin is marked by a strong, anticyclonic gyre centered around Zapiola Rise, called the Zapiola Anticyclone, and is located southeast of the BMC. In contrast to the edges of this gyre, the center is a region of relatively low kinetic energy (Artana et al., 2018).

Water masses in the Argentine Basin have typically been characterized using potential density (σ_θ) ranges, and the specific definitions vary somewhat among studies. However, the vertical layering between the surface and ∼2,000 m in all studies is essentially the same, with Subantarctic Surface Water (SASW) or South Atlantic Central Water (SACW) occupying the shallowest layer, followed by Subantarctic Mode Water (SAMW), Antarctic Intermediate Water (AAIW), and Circumpolar Deep Water (CDW). Some studies include finer classifications, with AAIW split into Upper, Central, and Lower varieties (with the additional caveat that Upper and Central AAIWs are classified as SAMW in some studies) and CDW similarly split into Upper CDW, CDW, and Lower CDW (Artana et al., 2018; Fontela et al., 2021; Maamaatuaiahutapu et al., 1994; Provost et al., 1995). For the purposes of this study, we have adopted the somewhat simpler classification of Fontela et al. (2021), wherein a "seasonal layer" is defined to extend from the surface to ∼100 m; SACW is defined to extend from the bottom of the seasonal layer to $\sigma_\theta = 26.5$ kg m^{-3}; SAMW occupies the potential density range from $\sigma_\theta = 26.5$ to $\sigma_\theta = 27.10$; and AAIW lies between $\sigma_\theta = 27.10$ and $\sigma_\theta = 27.40$ kg m^{-3}. Finer distinctions of these water masses and the inclusion of deeper water masses are beyond the scope of this study, as we are primarily concerned with the upper 0–400 m of the water column. In fact, an interesting similarity of many studies describing circulation and water masses in the Argentine Basin is that the top ∼100 m is often excluded from the analyses as it is labeled

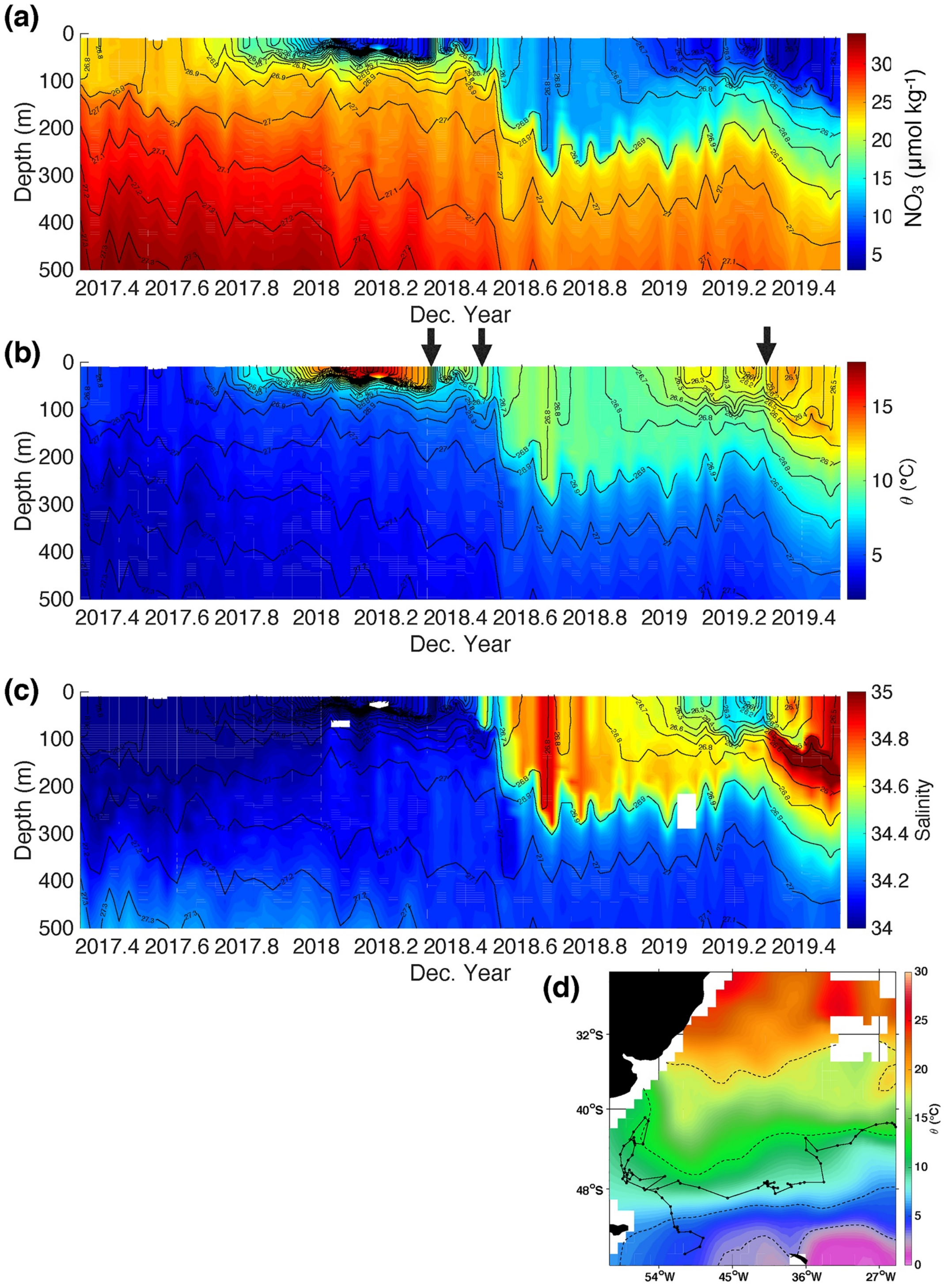

Figure 1. Float WMO 5904982 timeseries of (a) nitrate concentration (NO_3; µmol kg^{-1}), (b) potential temperature (θ; °C); and (c) salinity along the path of the float, restricted to 0–500 m depth range. The black contours represent potential density anomaly (σ_θ), with an interval of 0.1 kg m^{-3}. The black arrows in panel b denote the approximate times when the float crossed a front. (d) The position of the float over time, superimposed on a background of potential temperature at 10 m (closest, consistently available depth to sea surface). Dashed lines show the fronts/zone boundaries, defined by potential temperature at 100 m.

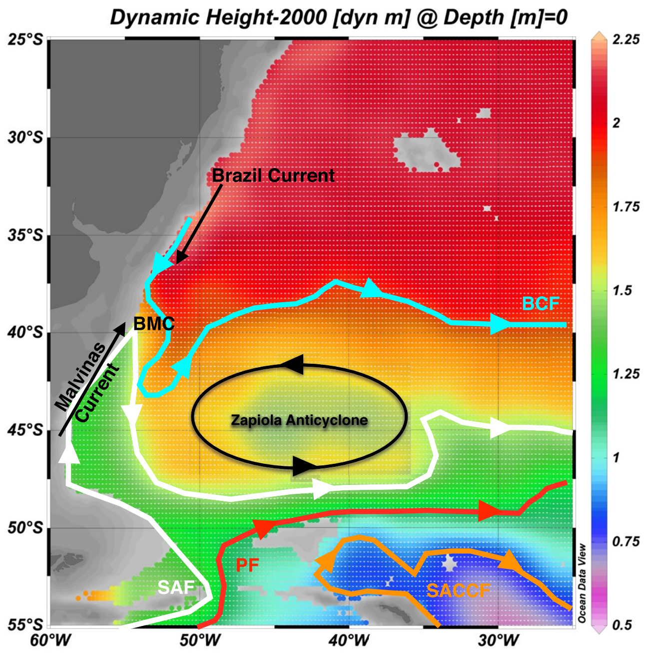

Figure 2. Dynamic height, referenced to 2,000 m, at the sea surface compiled from World Ocean Atlas 2013 Annual Data, 0.25° resolution (Schlitzer, 2014). Approximate positions of the Subantarctic Front (SAF, white), Polar Front (PF, red), Subantarctic Circumpolar Current Front (SACCF, orange), and Brazil Current Front (BCF, cyan) are shown as solid lines. Black arrows denote the general directions of the Malvinas Current, Brazil Current, and Zapiola Anticyclone. BMC = Brazil-Malvinas Confluence. Adapted from Artana et al. (2018).

a seasonally mixed layer with high temporal variability. However, it is this topmost layer where most of the net community production takes place and will be the primary focus of this study.

3. Data

The core-Argo program consists of an international fleet of autonomous profiling floats extending throughout the world ocean that has collected measurements of pressure, temperature, and salinity since its inception in 1999 and has since expanded (BGC-Argo) to include measurements of dissolved oxygen (O_2; starting in 2007) and other biogeochemical variables, including NO_3^-, chlorophyll fluorescence (chl F), pH, and optical backscatter (starting in 2014).

The general operating procedure of an Argo float is well-known and includes drifting at a pressure of ~1,000 db during "park" mode and then collecting a vertical profile through the water column every 10 days by first descending to ~2,000 db and then collecting measurements during its ascent to the surface. Once at the surface, the float obtains a fix on its position using GPS and then establishes communication via satellite to transmit data back to shore.

All float profiles are freely and publicly available via Global Data Assembly Centers (GDACs) as either near real-time files (R-files) that have undergone a series of automated quality control checks or delayed-mode files (D-files) that have been more thoroughly checked for errors and adjusted/recalibrated as needed (Argo, 2023); in the case of sensor errors or poor data quality, data is flagged accordingly. Two varieties of Argo floats were used in this study: (a) core Argo floats that measure only pressure, temperature, and conductivity and (b) BGC-Argo floats that also measure O_2, NO_3^-, chl F, and/or optical backscatter. A summary of the floats included in this study is given in Table 1.

Sensors on the floats included Seabird Scientific Druck 2900 pressure sensors, SBE41CP temperature and conductivity sensors, ISUS (In-Situ Nitrate Analyzer) nitrate sensors, and FLBBAP2 optical sensors (chl F and backscatter). Raw measurements of pressure are checked (and adjusted) via comparison with measurements at the sea surface (presumed equal to zero). The error is assigned an estimate of 2.4 db, unless the sensor has exhibited evidence of malfunction or failure (not applicable for the floats used in this study) (Wong et al., 2022). Temperature profiles are examined visually for errors and, unless the data are flagged as bad, are typically assigned an error estimate of 0.002°C (Wong et al., 2022). Salinity measurements are compared against objectively mapped estimates on a set of isotherms where the salinity variance is minimal (Wong et al., 2003, 2022). The mapping incorporates high quality CTD data from reference databases comprising both ship-based research cruises and previously deployed Argo floats that have passed a series of stringent quality control measures. Sensor calibration drift and offsets are determined via piecewise linear regressions in conductivity space. The median salinity error was 0.01, with 91% of measurements having an error <0.02 and 9% with an error >0.02. Measurements of NO_3^- are typically adjusted via comparison of measurements below 1,000 db (~1,500 db is the default depth of comparison) against reference data sets (e.g., GLODAPv2, World Ocean Atlas, and algorithms that estimate NO_3^- such as LINR (Carter et al., 2018) and CANYON-B (Bittig et al., 2018)); such adjustments are applied to the full profile as the vast majority of offsets and/or drift in the NO_3^- measurements are not depth-dependent (Johnson et al., 2013, 2017a; Maurer et al., 2021). The mean NO_3^- error ± one standard deviation from the floats used in this study was 0.89 ± 0.31 μmol kg^{-1}, where ~69% of measurements were associated with an error of <1 μmol kg^{-1} and ~31% were associated with an error >1 μmol kg^{-1}; the maximum recorded error estimate was 1.77 μmol kg^{-1}. We note that the limit of detection for the ISUS is 0.5 μmol kg^{-1} after correction of the absorbance spectrum for the effects of temperature and salinity (Maurer et al., 2021). We also note that the NO_3^- errors were not correlated with salinity errors; the NO_3^- concentration calculation requires salinity, but it is not very sensitive to salinity variations (T. Maurer, personal communication). Chlorophyll a (chla) concentrations were estimated from the fluorescence measurements collected by the sensors, after corrections for in-situ dark values and non-photochemical quenching (Roesler et al., 2017; Xing et al., 2012). Uncertainty in the chla concentrations is large, with a relative error

Table 1
Summary of the Different Floats From Which Data Was Compiled for This Study

		Min	Max	Min	Min	Max	Max	
WMO ID	Sensor package	Date	Date	Lat	Long	Lat	Long	No. profiles
1901385	Core	01/16/10	08/24/18	−60.493	−179.543	−40.613	178.755	310
1901411	Core	01/28/10	03/26/18	−63.849	−178.996	−44.632	179.434	294
1901413	Core	01/31/10	12/28/18	−59.807	−179.987	−40.519	179.577	321
1901415	Core	01/30/10	10/27/18	−62.356	−178.082	−36.416	179.930	315
2900108	Core	09/07/07	11/13/16	−58.847	−179.629	−46.981	179.315	330
2900133	Core	11/29/07	03/06/17	−65.277	−179.235	−35.247	6.894	334
5900696	Core	12/16/04	05/08/15	−60.685	−179.728	−39.670	179.145	360
5900702	Core	04/23/05	02/18/19	−58.819	−145.374	−35.885	73.091	480
5900703	Core	04/21/05	02/16/19	−63.536	−168.362	−42.049	133.662	479
5900704	Core	04/21/05	08/04/19	−59.005	−176.998	−36.174	−30.549	496
5900705	Core	04/29/05	10/20/18	−57.265	−142.785	−42.409	152.036	468
5900706	Core	04/28/05	02/23/19	−58.321	−137.868	−29.586	68.026	479
5900896	Core	04/25/05	10/17/18	−61.291	−137.249	−37.438	96.785	468
5900897	Core	04/22/05	10/27/16	−64.131	−162.786	−40.896	178.374	400
5900899	Core	04/26/05	05/29/17	−58.750	−128.283	−46.096	132.683	420
5900932	Core	05/03/05	01/17/19	−60.354	−169.715	−30.227	28.472	476
5900933	Core	05/03/05	09/13/18	−59.741	−178.973	−45.710	68.632	462
5901377	Core	10/07/07	11/14/17	−62.295	−177.059	−37.049	31.451	364
5901438	Core	09/06/07	11/02/16	−61.941	−179.055	−46.704	179.576	330
5902112	Core	01/08/09	09/18/12	−58.722	−81.572	−40.446	−37.039	273
5902133	Core	03/28/09	06/15/19	−46.991	−55.616	−27.956	33.488	367
5903417	Core	11/11/13	12/17/19	−42.356	−51.553	−34.177	−12.643	220
5903573	Core	11/06/13	05/22/20	−33.157	−40.149	−27.562	−18.296	236
5903581	Core	11/11/13	09/27/21	−56.451	−56.105	−30.739	165.398	284
5903605	Core	11/08/13	02/12/19	−44.593	−54.892	−30.707	−29.959	190
5903710	Core	11/09/13	02/02/18	−40.128	−42.060	−29.734	−23.718	153
5903725	Core	11/09/13	01/02/18	−47.980	−55.031	−32.294	−35.403	150
5903728	Core	11/08/13	04/03/19	−46.013	−52.937	−25.810	−19.738	188
5903729	Core	11/05/13	04/21/20	−41.437	−52.378	−27.934	−8.578	233
5903731	Core	11/10/13	10/14/18	−44.192	−53.260	−31.266	−16.193	177
5904103	Core	03/05/13	08/26/18	−61.996	−179.300	−47.004	179.062	285
5904118	Core	11/11/13	05/16/18	−42.278	−53.784	−32.668	−23.608	163
5904120	Core	11/08/13	06/02/18	−40.419	−42.298	−29.558	−27.450	165
5904122	Core	11/07/13	08/23/19	−44.809	−52.001	−31.525	−4.836	209
5904142	Core	11/10/13	08/16/19	−48.624	−55.361	−24.650	27,000	208
5904144	Core	11/05/13	06/21/19	−36.137	−27.996	−30.804	−11.939	203
5904151	Core	12/12/13	07/24/18	−65.694	−124.540	−54.835	−39.064	241
5904155	Core	12/12/13	02/04/19	−67.736	−127.971	−41.667	−33.259	268
5904169	Core	11/07/13	08/11/18	−33.786	−45.240	−24.777	−16.963	172
5904170	Core	11/05/13	01/11/22	−48.744	−54.450	−25.975	−7.944	294
5904185	NO_3, chl	04/07/14	11/15/18	−64.156	−149.928	−51.523	−49.352	164
5904475	NO_3, chl	12/05/14	03/07/20	−39.612	−25.445	−26.713	14.451	202

Table 1
Continued

WMO ID	Sensor package	Min Date	Max Date	Min Lat	Min Long	Max Lat	Max Long	No. profiles
5904657	NO_3	01/10/16	07/13/20	−56.789	−57.205	−43.076	4.988	160
5904658	NO_3	01/09/16	08/11/20	−58.858	−57.354	−36.376	24.371	163
5904659	NO_3, chl	01/08/16	04/30/20	−59.845	−55.383	−48.347	51.726	153
5904660	NO_3, chl	01/07/16	04/20/20	−60.640	−54.635	−45.783	−3.685	152
5904661	NO_3, chl	12/29/15	05/30/20	−58.275	−89.735	−39.140	−14.340	157
5904662	NO_3	12/29/15	03/31/18	−58.396	−89.709	−47.885	−36.174	84
5904695	NO_3	05/14/16	02/14/21	−58.337	−169.949	−43.347	−32.659	169
5904845	NO_3, chl	01/20/17	10/15/21	−61.220	−102.937	−45.688	43.631	173
5904848	Core	01/19/17	05/15/20	−59.214	−102.586	−51.255	−33.769	242
5904854	NO_3, chl	12/28/16	12/07/20	−57.349	−68.005	−40.090	37.198	144
5904856	NO_3, chl	12/30/16	07/14/20	−64.140	−69.096	−49.282	−14.647	129
5904980	NO_3, chl	01/02/17	03/05/20	−66.781	−74.241	−53.674	−29.873	115
5904982	NO_3, chl	12/28/16	01/27/21	−59.210	−69.403	−40.901	−3.768	149
5904984	NO_3, chl	12/29/16	06/22/20	−62.045	−68.697	−54.755	−26.444	128
5905066	Core	01/05/17	05/26/22	−69.183	−99.837	−37.417	−6.137	190
5905076	NO_3, chl	02/22/17	07/31/21	−59.927	−126.307	−40.839	−35.560	162
5905077	NO_3, chl	02/18/17	04/18/21	−67.634	−125.902	−48.358	−31.349	152
5905079	NO_3, chl	02/23/17	10/24/20	−59.552	−125.677	−36.260	−48.238	133
5905098	Core	04/27/17	06/18/22	−65.218	−179.979	−51.635	179.246	180
5905132	NO_3, chl	10/06/17	11/11/20	−36.819	−25.385	−30.638	−8.142	69
5905141	Core	10/24/17	01/13/22	−36.454	−47.571	−32.377	−25.283	314
5905142	Core	10/26/17	08/11/21	−39.306	−44.114	−28.895	−27.569	280
5905145	Core	10/23/17	06/05/22	−48.670	−58.989	−28.548	−25.877	160
5905146	Core	10/25/17	06/07/22	−39.197	−29.550	−32.537	−20.447	161
5905980	NO_3, chl	10/19/18	02/21/21	−28.424	−45.199	−22.679	−28.314	86
5905981	NO_3, chl	10/19/18	06/13/20	−28.548	−42.028	−26.719	−28.317	61
5905982	NO_3, chl	10/21/18	05/10/22	−45.578	−55.119	−29.543	−33.659	129
5905983	NO_3, chl	10/22/18	05/13/22	−40.942	−41.780	−33.627	−31.295	130
5905984	NO_3, chl	10/24/18	05/14/22	−51.534	−41.356	−38.271	−3.126	131
5905985	NO_3, chl	10/25/18	05/13/22	−41.843	−44.325	−35.770	−24.383	129
5905991	NO_3, chl	01/28/19	05/06/22	−64.172	−47.479	−54.121	−15.274	120
5906003	NO_3, chl	03/03/19	09/11/21	−60.121	−51.616	−53.362	−10.731	93
5906213	NO_3, chl	12/07/19	05/12/22	−59.146	−90.113	−39.197	−48.299	87
5906215	NO_3	01/07/20	01/01/21	−58.521	−83.355	−48.460	−47.388	36
5906216	NO_3	12/22/19	12/01/21	−59.002	−88.925	−36.169	−33.875	70
5906217	NO_3	12/29/19	05/11/22	−60.460	−88.945	−39.827	−34.298	85
5906224	NO_3	01/30/20	12/02/21	−62.928	−82.094	−41.041	−53.481	66
5906330	Core	12/27/20	07/12/22	−57.950	−68.390	−40.242	−32.550	56
5906332	Core	12/27/20	07/12/22	−58.563	−67.723	−34.503	−41.464	56
5906333	Core	12/28/20	02/10/22	−60.433	−64.575	−49.596	−40.865	40
5906334	Core	12/28/20	02/09/22	−59.439	−65.973	−39.443	−42,000	41
5906335	Core	12/28/20	02/02/22	−59.969	−65.221	−51.977	−39.557	36

Table 1
Continued

WMO ID	Sensor package	Min Date	Max Date	Min Lat	Min Long	Max Lat	Max Long	No. profiles
Total								18,002
Total core								14,021
Total BGC								3,981

of 50%; however, we note that chla is used in a mostly qualitative manner in this study, specifically to identify the depth of the maximum value in each profile. Further details explaining the quality assessment and quality control of pressure, temperature, and salinity are available in Wong et al. (2020). Details regarding the quality control and calibration of O_2 and NO_3^- data are provided in Maurer et al. (2021).

4. Results and Discussion

4.1. Defining Hydrographic Fronts/Zones

Artana et al. (2018) has previously defined major oceanographic fronts in the Argentine Basin using σ_θ at 450 m depth. Four fronts were described in their study: BCF defined at $\sigma_\theta = 27$ kg m^{-3} (separating SACW and SASW from Upper AAIW); Main SAF defined at $\sigma_\theta = 27.15$ kg m^{-3} (separating Upper from Central AAIW); North PF defined at $\sigma_\theta = 27.27$ kg m^{-3} (separating Central from Lower AAIW); and Main PF defined at $\sigma_\theta = 27.33$ kg m^{-3} (separating Lower AAIW from Upper CDW).

All available temperature and salinity data from the Argo floats listed in Table 1 were compiled to produce a map of density at 450 m and, using the front definitions supplied by Artana et al. (2018), classify all of the individual profiles into one of five zones, labeled (moving from south to north), Zones D1, D1.5, D2, D3, and D4 (Figure 3, left panels). The zones were named with a preceding "D" to specify that they were defined using σ_θ at 450 m; the numbering of the zones is meant to facilitate comparisons with zones defined using potential temperature (θ) at 100 m that occupy a similar area (see below). The results were reasonably comparable with those of Artana et al., although there were some significant overlaps among zones, particularly between Zones D2 and D3. In addition, Zone D1.5 was represented by fewer profiles compared to the other zones and occupied a narrow strip of space between Zones D1 and D2.

We were interested in determining whether these frontal definitions would be appropriate for splitting up the study area with the purpose of estimating NCP. As the majority of photosynthesis is expected to take place well above 450 m, we compared the σ_θ distribution at 450 m against that at 100 m (the lower limit of the "seasonal layer" i.e., typically ignored in water mass studies of this region). Furthermore, we opted to use θ rather than σ_θ for defining fronts (and zones) as temperature sensors on Argo floats are less prone to drift and failure (compared to conductivity cells). Although conductivity cell failure is relatively rare on Argo floats, the use of temperature instead of density would potentially enable users to separate float data into zones and estimate NCP from biogeochemical data from any such float with a failed conductivity cell. Furthermore, a focus on temperature may be more universally applicable to other arrays, autonomous vehicles, and archives of XBTs that lack conductivity measurements (or are relatively lacking in quality) for defining hydrographic fronts in the Argentine Basin. A comparison of σ_θ (Figure S1 in Supporting Information S1) and θ (Figure S2 in Supporting Information S1) distributions at both 450 and 100 m is provided in the Supporting Information; we also note that σ_θ and θ at both 450 and 100 m are highly correlated (Figure S3 in Supporting Information S1), further justifying this choice.

The distribution of θ at 100 m (Figure 3, right panels) exhibits similar gradations as the σ_θ distribution at 450 m (Figure 3, left panels), with the general positions and alignments of large gradients/fronts also being quite similar (but not exact) between the two distributions. There also appears to be an additional front in θ at 100 m, aligned approximately along the 32°S latitude line, that is not apparent in the σ_θ at 450 m density distribution. The fronts were defined by visual selection of temperature difference across each front, with some trial and error to minimize overlap across frontal boundaries. However, these selections were supported by meridional gradients calculated from the θ field since bands of maximum gradients were generally aligned along the selected isotherms defining the fronts (Figure S4 in Supporting Information S1). Thus, five zones were defined using specified θ ranges at 100 m:

$$\text{Zone T1}: \theta \leq 3^\circ\text{C (Southernmost, Antarctic Zone)}$$

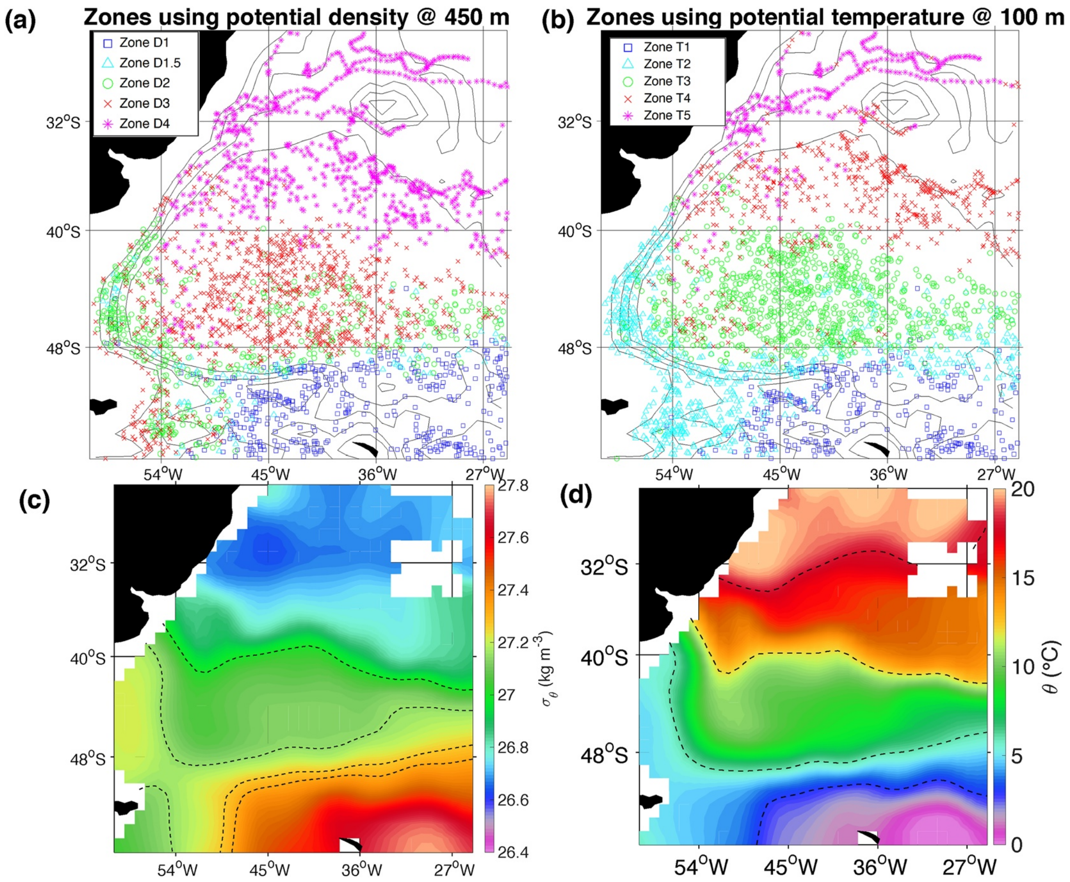

Figure 3. Comparison of hydrographic zones, separated by frontal boundaries defined using potential density at 450 m versus potential temperature at 100 m. (a) Profiles separated based on the potential density: Zone D1 (blue squares), Zone D1.5 (cyan triangles), Zone D2 (green circles), Zone D3 (red squares), and Zone D4 (magenta stars). (b) Profiles separated based on potential temperature: Zone T1 (blue squares), Zone T2 (cyan triangles), Zone T3 (green circles), Zone T4 (red squares), and Zone T5 (magenta stars). (c) Potential density anomaly (kg m^{-3}) at 450 m; dashed lines show the fronts/zone boundaries, defined by potential density at 450 m. (d) Potential temperature (°C) at 100 m; dashed lines show the fronts/zone boundaries, defined by potential temperature at 100 m.

$$\text{Zone T2} : 3 < \theta \leq 6^{\circ}\text{C (Southwestern/Coastal Zone)}$$

$$\text{Zone T3} : 6 < \theta \leq 12^{\circ}\text{C (Transition Zone)}$$

$$\text{Zone T4} : 12 < \theta \leq 18^{\circ}\text{C (North of BCF)}$$

$$\text{Zone T5} : \theta > 18^{\circ}\text{C (Northernmost, Subtropical Zone)}$$

where the preceding "T" designates these zones as defined using θ at 100 m. While the numbering of the zones is meant to facilitate comparisons with the closest corresponding zones using the σ_θ at 450 m definitions, Zone D1.5 and Zone T5 were enumerated separately as they did not closely correspond (in space) with a zone using the other method. We briefly note that θ and NO_3^- concentrations at 10 m (near the sea surface), 200 m, and 300 m were also considered to define fronts (Figure S5 in Supporting Information S1). Each of these distributions exhibited numerous similarities in the general positions of fronts; however, we found that the θ at 100 m provided front definitions that resulted in the least overlap among zones.

The next topic to address is whether there are enough data within each zone to estimate NCP via seasonal drawdown of NO_3^-. It is apparent from Figure 4b that the spatial coverage over any one zone was not sufficient for an assessment of interannual variability; however, there was sufficient spatial coverage over each zone to analyze monthly variations (Figures 4a and 4d), albeit averaged across five years of observations (2016–2021). We have

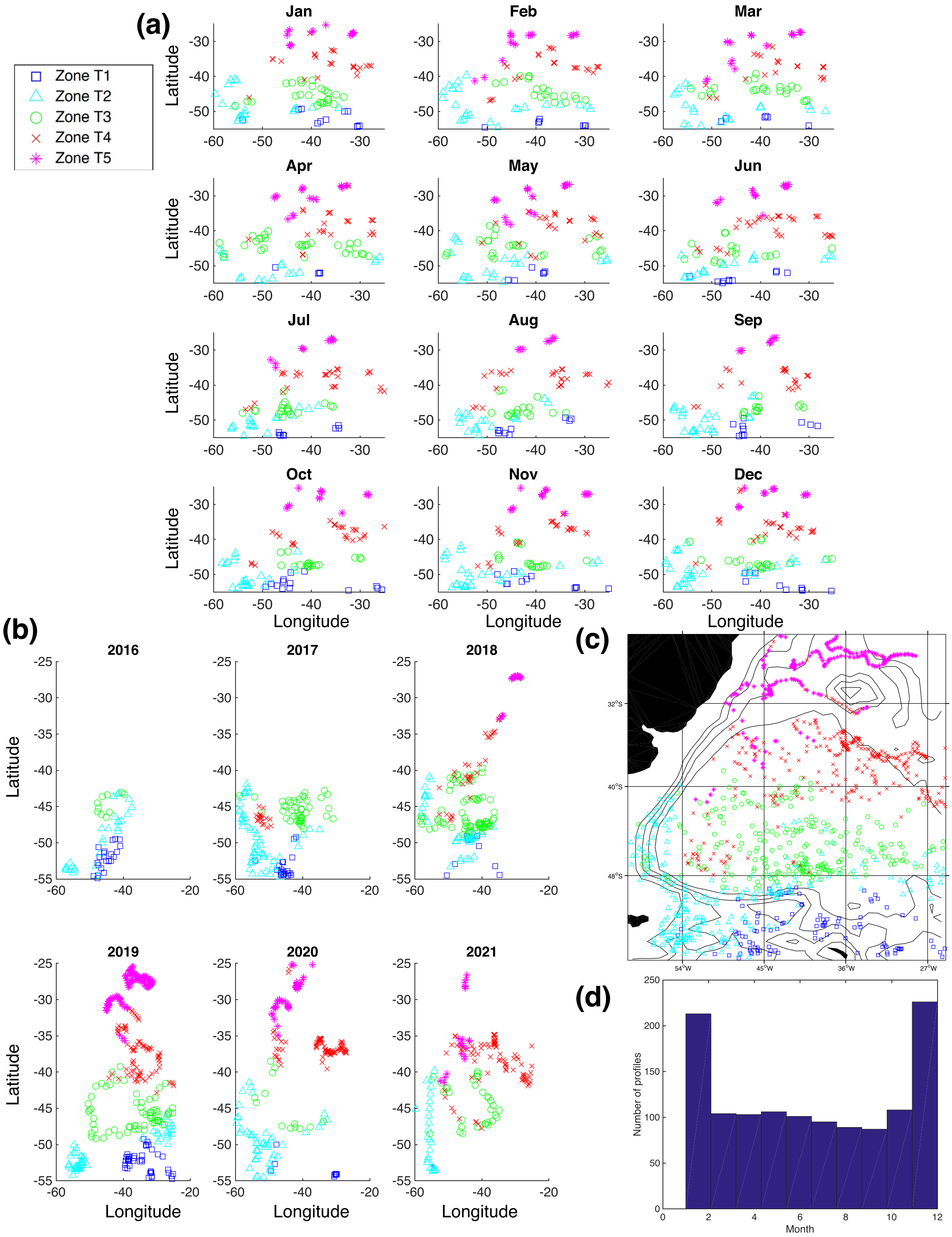

Figure 4. (a) Monthly maps of biogeochemical profile positions in each of the five zones defined using potential temperature at 100 m: Zone T1 (blue squares), Zone T2 (cyan triangles), Zone T3 (green circles), Zone T4 (red squares), and Zone T5 (magenta stars). (b) Annual maps of biogeochemical profiles divided into Zones T1-T5. (c) Map of all available biogeochemical profiles, divided by zone. (d) Histogram showing the number of biogeochemical profiles available for each month.

therefore sought to estimate NCP within each zone via construction of median monthly vertical profiles of NO_3^- and calculation of seasonal changes in the NO_3^- inventory integrated over a specified depth range. The available spatial coverage should allow for the monthly binned profiles to reasonably represent the median NO_3^- concentrations characteristic of each zone during each month.

4.2. Seasonal Progression of NO_3^- and Chla

All available data within the defined zones were separated by month and then organized into 20 m bins between the surface and 500 and 100 m bins between 600 and 2,000 m to construct representative, monthly profiles of nitrate for each zone using both the σ_θ at 450 m (Zones D1-D4) and θ at 100 m (Zones T1-T5) front definitions (Figure S6 in Supporting Information S1). Median NO_3^- concentrations were calculated for each depth bin instead of using means to minimize biases resulting from anomalous/extreme concentrations within a specified bin across each zone. The monthly median profiles were then plotted as timeseries for each zone to evaluate the seasonal progression of NO_3^- concentrations in the upper 0–400 m of the water column (Figure 5). We note that the reduction of the available data into monthly profiles representing each zone smooths over episodic upwelling, mesoscale activity, and other, smaller scale features that might ultimately underestimate NCP. However, we believe this approach establishes a baseline method for computing NCP from available BGC-Argo data that may be built upon to further understand the impacts of smaller temporal and spatial scale events on NO_3^- uptake and NCP.

Monthly mixed layer depths (MLDs), calculated as a difference of 0.2 °C from the potential temperature averaged over 0–10 m (Munro et al., 2015; Stephenson et al., 2012), were also plotted to visualize how the deepening and shoaling of the mixed layer in winter and summer corresponded in time with variations in NO_3^- concentrations. Finally, similarly binned, monthly profiles of chla concentration from those floats that were equipped with the necessary sensors were also plotted to track the timing and vertical scope of primary production in each zone.

The MLDs (dashed, white lines) showed a progression from shallower depths during January-April, deepening to maximum depths between July and September, and subsequent shoaling between September and December. In general, NO_3^- concentrations were higher during austral winter, approximately between June and September, with lower NO_3^- concentrations during austral spring and summer (November through April). However, NO_3^- concentrations in the top 0–100 m exhibited somewhat different progressions among the different zones. In Zones T1 (Figure 5k) and T2 (Figure 5l), NO_3^- concentrations began to increase within the mixed layer as early as April and continued to increase as the mixed layer deepened. In Zone T1, chla concentrations (Figure 5p) appeared to remain relatively low until January whereas chla concentrations in Zone T2 (Figure 5q) started to increase in August and September, soon after the mixed layer began to shoal. In both Zones T1 and T2, NO_3^- concentrations reached lowest levels (but still replete) of ∼16 μmol kg^{-1} by December and remained relatively consistent until April; chla concentrations also remained relatively high and focused in the top 0–50 m until April. Similar progressions were observed in Zones D1, D1.5, and D2 (Figure 5a–5c).

Zones T3 (Figures 5m and 5r) and D3 (Figures 5d and 5i) exhibited similar progressions in both NO_3^- and chla as Zones T2 and D2, but NO_3^- concentrations were lower overall and did not appear to increase within the mixed layer until July or August. Concentrations of NO_3^- were even lower in Zones T4 (Figure 5n) and D4 (Figure 5e), with mixed layer concentrations reaching a maximum of ≤4 μmol kg^{-1} in August and decreasing to near zero concentrations by December. There was a persistent chla signal in the subsurface, centered around ∼100 m, but highest chla concentrations were still typically observed in the top 0–50 m, with maximum concentrations occurring between September and November (Figures 5j and 5s).

Subsurface chla maxima persisted between 100 and 150 m throughout most of the year in Zone T5 (Figure 5t) as NO_3^- concentrations (Figure 5o) remained below ∼2 μmol kg^{-1} throughout the top 0–100 m (where data were available). In contrast to the other zones, the maximum chla concentrations (while quite low) occurred between December and March; however, an increase in near-surface chla was observed between June and September during the period of mixed layer deepening.

4.3. Estimating NCP

Estimations of NCP were computed by constructing monthly, median vertical profiles of NO_3^- representative of each zone, integrating these profiles between the surface and an appropriate bottom depth to obtain monthly

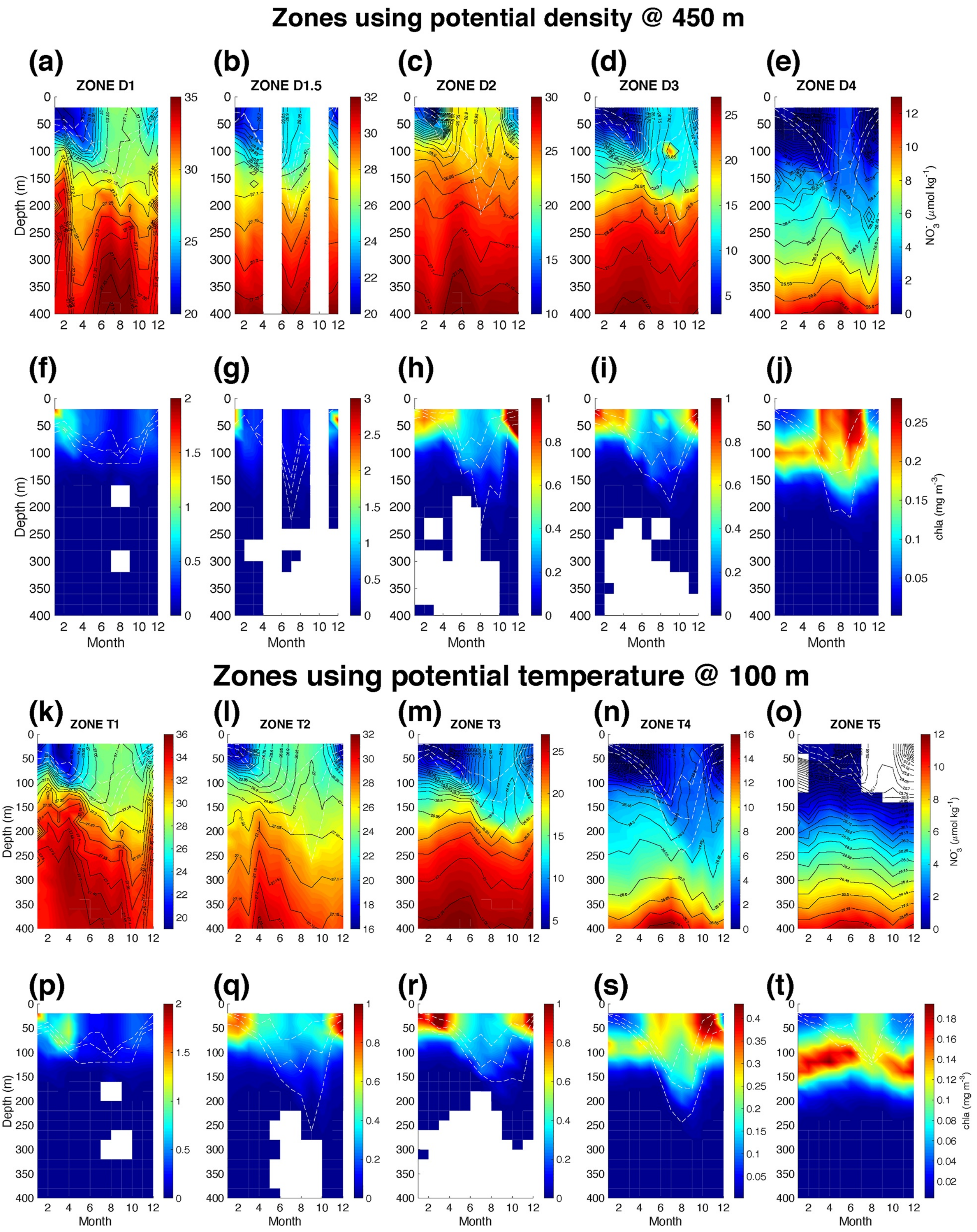

Figure 5. Timeseries of monthly median profiles of nitrate (NO$_3$; µmol kg^{-1}) and chlorophyll a (chla; mg Chl m^{-3}) concentrations from each of the five zones defined using potential density at 450 m (panels a–j) and potential temperature at 100 m (panels k–t). Black, solid lines denote contours of potential density anomaly (σ_θ), with an interval of 0.05 kg m^{-3}. The white, dashed lines denote the 25th, 50th (median), and 75th quartiles of the monthly mixed layer depth for each zone. The white patches indicate the lack of nitrate measurements for the corresponding depth ranges and months in the associated zones. Note the different scales of the colorbars used in each panel.

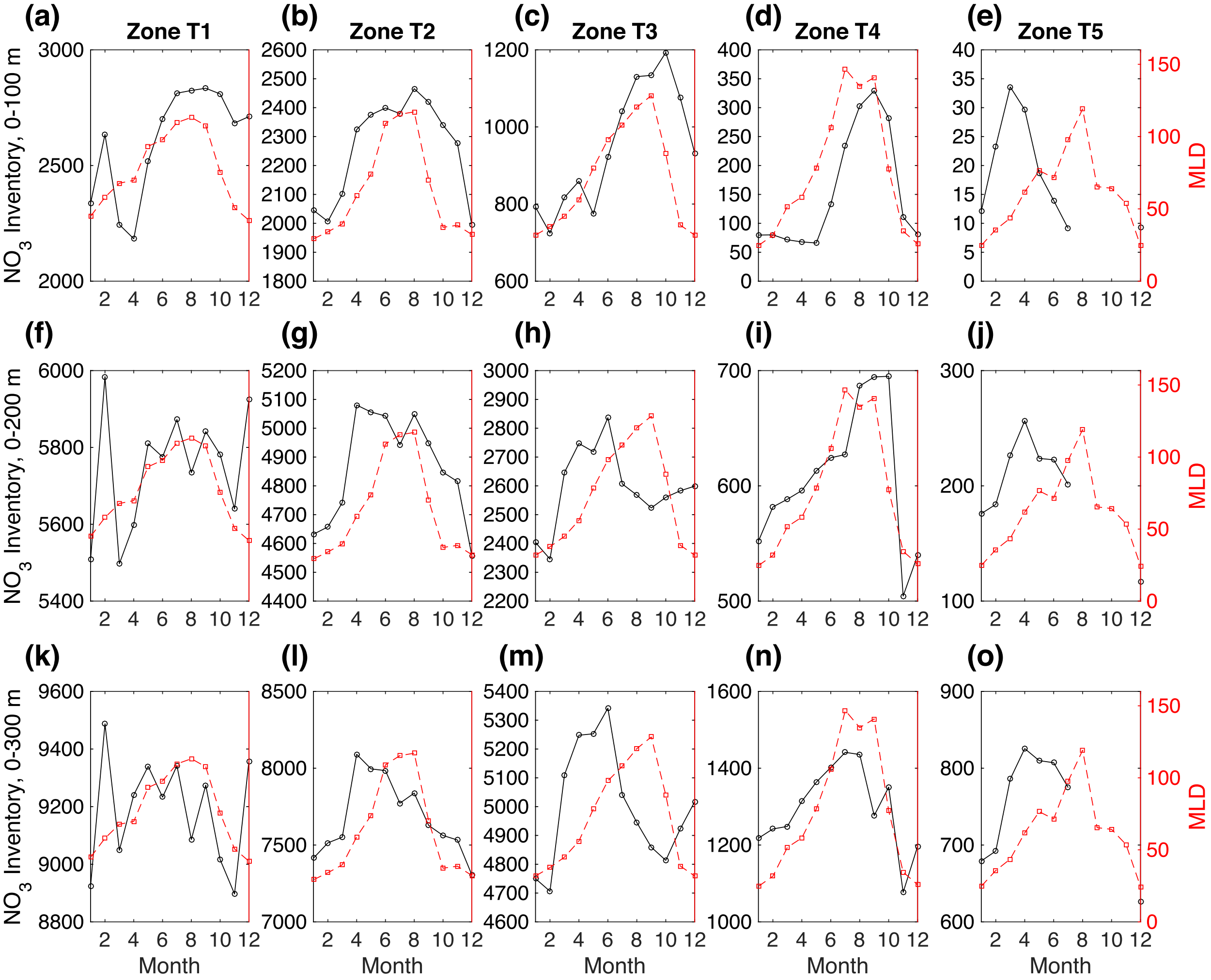

Figure 6. Monthly median nitrate inventories (mmol m^{-2}) calculated using the corresponding monthly median vertical profiles of nitrate concentration for each of the five zones defined using potential temperature at 100 m. Inventories for each zone are organized as separate columns. The top panels show inventories of nitrate integrated over 0–100 m (a–e), middle panels show inventories computed over 0–200 m (f–j), and bottom panels show inventories computed over 0–300 m (k–o). Note that each panel has two *y*-axes. The right axes correspond to the monthly median mixed layer depths (MLDs), in meters, in each zone (red squares connected by dashed lines); the scales of these axes are constant over all panels. The left axes correspond to the inventories computed over 0–100 m, 0–200 m, or 0–300 m in each zone (black circles connected by solid lines); the scale of each axis is different for each panel to show the seasonal progression of the nitrate inventory.

NO_3^- inventories, calculating the seasonal drawdown of NO_3^- using these inventories, and then converting this drawdown to NCP using the Redfield ratio (C/N = 6.6).

First, monthly median profiles were integrated between the surface and three different bottom depths (100 m, 200 m, and 300 m; see Figure 6) to obtain monthly NO_3^- inventories for each zone. The three bottom depths were explored to determine which depth might be most appropriate for each zone. Ideally, the bottom depth would be deep enough to include the chla maximum (to ensure all production is accounted for) and shallow enough to exclude any isopycnal heaving that might bias the results. For example, relatively high NO_3^- concentrations (>34 μmol kg^{-1}) were present at ~120 m in Zone T1 between January and April, associated with isopycnals of 27.2–27.3 kg m^{-3} (Figure 5k). However, these isopycnals (and higher NO_3^- concentrations) deepened to > 200 m between May and October. As a result of this isopycnal heaving, NO_3^- inventories integrated over the 0–200 and 0–300 m depth ranges will be biased high between January and March relative to subsequent months.

We explore these potential biases by comparing integrals of 0–100 m, 0–200 m, and 0–300 m against the monthly median MLDs in each zone (Figure 6). In Figure 6, the solid, black lines show the NO_3^- inventories computed for 0–100 m (top panels), 0–200 m (middle panels), and 0–300 m (bottom panels) for Zones T1-T5 (different columns). The magnitude of these inventories vary greatly, so the scales of the left *y*-axes differ in each panel. The mixed layer depths for each zone (red, dashed lines) are also shown in each panel with identical scales that are separate (right *y*-axes) from those of the deeper inventories. If we assume that the deepening and shoaling of the mixed layer is highly correlated to the available NO_3^- inventory in each zone (via entrainment of deep NO_3^- into the mixed layer during winter mixing and drawdown of NO_3^- during spring and summer once the mixed layer shoals), then substantial deviations between the NO_3^- inventories and the MLD might be attributed to processes at depth (e.g., isopycal heaving) that could bias the NCP estimates. Although there are no perfect matches, the minimum and maximum NO_3^- inventories are in reasonably good agreement with minimum and maximum MLDs, except for Zone T5 (where there was a persistent, deep chla maximum below the mixed layer) and the deeper (0–200 m and 0–300 m) integrals in Zones T1-T3. Such mismatches mostly result from shoaling/upwelling of deeper waters with higher NO_3^- concentrations that do not necessarily impact NCP. Therefore, the NO_3^- inventories computed over 0–100 m were utilized to estimate NCP for Zones T1-T3 (and similarly, Zones D1, D1.5, D2, and D3). In contrast, isopycnal heaving was much less pronounced in Zones T4, T5, and D5 and, since chla maxima were present below 100 m in these zones (Figure 6j, s, and t), NO_3^- inventories computed over 0–200 m were utilized to estimate NCP in these zones. We briefly note that a comparison of NO_3^- inventories calculated over the MLD showed a very similar seasonal pattern as the MLDs themselves (see Figure S7 in Supporting Information S1), lending further support to our assumptions.

Next, three different methods for estimating the seasonal drawdown of NO_3^- were explored. The first method was employed by Johnson et al. (2017b) to compute NCP in the Southern Ocean from NO_3^- measurements on BGC-Argo floats. They found profiles with the highest and lowest NO_3^- during austral winter (August-November) and summer (December-March), then estimated the mean vertical profile of NO_3^- for the months corresponding to the maximum and minimum nitrate and subtracted the resulting integrals. Here, we have identified the months with the highest and lowest NO_3^- inventories for each zone and subtracted them to estimate the NCP (Table 2).

A second method we employed was to subtract the mean NO_3^- inventories for austral winter, taken in this case as July-October, and the mean inventories for austral summer, taken as December-March (Table 2). The choices regarding which months to include as winter and summer months were based on the monthly profiles for each zone. The NCP estimates derived from this method were lower than those estimated from the maximum minus minimum method by 0.6–2.1 mol C m^{-2}, with the largest discrepancy occurring in Zone T1. This is not entirely surprising as the maximum minus minimum method is expected to yield an estimate of maximum NCP from the available data (Johnson et al., 2017b).

The third method we tested was the use of simple linear regression to estimate NO_3^- drawdown from austral winter/spring (August-November) through the summer (December-March). Note that a regression could not be completed for Zone 5 due to limited data. The NCP estimates from this method were quite similar to the maximum minus minimum method. We briefly note that the comparison of the NCP estimates across the three methods, while imperfect, were in reasonably good agreement for the integration depths chosen. The use of different integration depths (e.g., 0–300 m for Zone T4 instead of 0–200 m) resulted in larger discrepancies in the NCP estimates using the three different methods. Such comparisons may therefore prove valuable as they can help to guide decisions in choosing integration depths for calculating NCP in future studies.

The resulting NCP estimates suggest a mean NCP of 3–4 mol C m^{-2} yr^{-1} for the Argentine Basin south of 40ºS and a substantial decrease to ~1 mol C m^{-2} yr^{-1} north of 40ºS. The relatively low NCP estimate for Zone D1.5 may have been a consequence of the limited number of profiles within this very narrow zone.

4.4. Comparing NCP Estimates With Independent Studies

Based primarily on surface measurements of nutrients, dissolved inorganic carbon (DIC), and pCO_2 from ships of opportunity traversing the Drake Passage between 2002 and 2011, Munro et al. (2015) estimated annual NCP of 1.2 ± 0.7 and 1.6 ± 0.4 mol C m^{-2} yr^{-1}, approximately half of the estimates reported in this study. However, their study focused mostly on NCP within the mixed layer and collected data from a region (56°–64°S, 56°–68°W) located both southward and westward of the Argentine Basin. Still, due to the close proximity of the two study areas and the continuation of the SAF and PF from the Drake Passage into the Argentine Basin, one might expect similar rates of NCP in the southernmost zones. The mean, spring-summer MLDs across Munro et al.'s four subregions ranged between 49 and 62 m; therefore, the difference in depth ranges considered for the NCP calculations might explain the discrepancies in NCP estimates at similar latitudes.

Table 2

Net Community Production (NCP) Estimates for the Different Zones Defined Using Potential Temperature at 100 m Versus Those Defined Using Potential Density at 450 m Using Three Different Methods to Compute the Seasonal Drawdown of the Nitrate Inventory Over 0–100 or 0–200 m Depth: (a) Max-Min, (b) Avg Winter-Avg Summer, and (c) Slope (Linear Regression)

Potential temperature @ 100 m zones						Potential density @ 450 m zones					
Integration depth	100 m	100 m	100 m	200 m	200 m	Integration depth	100 m	100 m	100 m	100 m	200 m
Zone	T1	T2	T3	T4	T5	Zone	D1	D1.5	D2	D3	D4
January	2,336.5	2,045.2	792.2	551.9	175.9	January	2,357.8	2,278.3	1,873.4	810.8	363.3
February	2,634.4	2,006.6	724.6	581.7	183.9	February	2,398.8	2,293.1	1,788.8	686.2	408.8
March	2,244.4	2,101.1	817.1	588.4	226.4	March	2,334.3	2,336.1	1,754.7	719.0	414.7
April	2,183.3	2,324.2	859.2	595.9	256.5	April	2,334.2	2,326.1	1,990.8	752.6	399.8
May	2,517.3	2,375.2	774.2	613.0	223.8	May	2,446.6		2,325.1	704.3	369.6
June	2,702.2	2,399.0	921.9	624.4	222.6	June	2,687.2	2,461.8	2,355.1	901.5	392.1
July	2,812.6	2,379.3	1,039.9	627.2	201.3	July	2,812.6	2,500.0	2,271.6	1,173.7	444.7
August	2,824.3	2,465.6	1,130.4	686.6	–	August	2,824.3	2,485.4	2,357.3	1,162.1	566.1
September	2,833.9	2,419.0	1,133.9	694.5	–	September	2,833.0	2,541.1	2,259.5	1,328.2	564.2
October	2,809.3	2,339.4	1,193.0	695.1	–	October	2,805.1		2,314.6	1,185.8	424.1
November	2,683.6	2,276.2	1,075.2	504.4	–	November	2,662.1	2,492.2	2,002.3	1,174.7	275.7
December	2,711.4	1,993.9	932.2	539.8	117.0	December	2,637.2	2,345.2	1,845.7	1,008.0	408.8
Max	2,833.9	2,465.6	1,193.0	695.1	256.5	Max	2,833.0	2,541.1	2,357.3	1,328.2	566.1
Min	2,183.3	1,993.9	724.6	504.4	117.0	Min	2,334.2	2,278.3	1,754.7	686.2	275.7
NCP (mol C m^{-2}), max-min	**4.3**	**3.1**	**3.1**	**1.3**	**0.9**	NCP (mol C m^{-2}), max-min	**3.3**	**1.7**	**4.0**	**4.2**	**1.9**
unc (mol C m^{-2})	***0.5***	***0.4***	***0.7***	***0.2***	***0.6***	unc (mol C m^{-2})	***0.1***	***0.4***	***0.2***	***1.1***	***0.6***
Winter	2,820.0	2,400.8	1,124.3	675.8	–	Winter	2,818.8	2,508.8	2,300.8	1,212.5	499.8
Summer	2,481.7	2,036.7	816.5	565.4	–	Summer	2,432.0	2,313.2	1,815.7	806.0	398.9
NCP (mol C m^{-2}), winter-summer	**2.2**	**2.4**	**2.0**	**0.7**	–	NCP (mol C m^{-2}), winter-summer	**2.6**	**1.3**	**3.2**	**2.7**	**0.7**
unc (mol C m^{-2})	***1.5***	***0.5***	***0.7***	***0.3***	–	unc (mol C m^{-2})	***0.9***	***0.3***	***0.5***	***1.1***	***0.5***
Slope (mmol m^{-2} mo^{-1})	−65.59	−59.72	−50.88	−15.17	–	slope (mmol m^{-2} mo^{-1})	−55.37	−25.09	−77.31	−47.17	−10.16
NCP (mol C m^{-2}), LINEAR REGRESSION	**3.9**	**3.5**	**3.0**	**0.9**	–	NCP (mol C m^{-2}), linear regression	**3.7**	**1.7**	**5.1**	**3.1**	**0.7**
unc (mol C m^{-2})	***2.4***	***1.8***	***1.9***	***1.1***	–	unc (mol C m^{-2})	***2.0***	***1.0***	***1.5***	***2.8***	***1.3***
NCP AVG (three methods)	**3.5**	**3.0**	**2.7**	**1.0**	**0.9**	NCP avg (three methods)	**3.2**	**1.6**	**4.1**	**3.3**	**1.1**

Note. The mean of these three methods is provided at the bottom of the table. Uncertainties (unc) in the NCP estimates were derived from: (a) difference in NCP computed when the second highest and lowest nitrate inventories are used instead of the maximum and minimum, (b) the standard deviations of winter and summer means and, (c) 95% confidence intervals in the determination of the slope.

Hennon et al. (2016) used measurements of O_2 from Argo floats to estimate respiration below the mixed layer and then related this respiration to the carbon export below ∼100 m. One or more of the floats included in that study passed through the Drake Passage and into the southern Argentine Basin; from these data, they estimated an export of 4.4 ± 2.9 mol C m^{-2} yr^{-1}. At steady state, the annual export is expected to be equivalent to the NCP; thus, the export estimate of Hennon et al. is relatively close to the NCP estimate from Zone T1 (this study). However, we note that the Hennon et al. study ignored the potential impact of advection through horizontal gradients, as they argued floats were likely to drift through both positive and negative gradients. This assumption may not be applicable in a region of strong hydrographic fronts, such as the Argentine Basin, but it was not clear whether the float(s) analyzed in their study crossed any fronts.

Schlitzer (2002) utilized an inverse modeling approach that varied circulation, air-sea fluxes, production and remineralization in a coupled, global circulation and biogeochemical model to determine optimal fits between the simulated fields and global data sets of temperature, salinity, O_2, nutrients, DIC, and total alkalinity and estimate export production and carbon fluxes. They reported that the most productive regions in the global ocean included the tropical Indian and Pacific Oceans, coastal upwelling regions of Chile, Peru, and Namibia, the Patagonian/Argentine shelf, and the Antarctic zonal band between 40°S and 60°S. The Patagonian shelf was also found to be an area of relatively high export production, with values up to 80 g C m^{-2} yr^{-1} (∼6.7 mol C m^{-2} yr^{-1}); the 40°–60°S zonal belt of the Southern Ocean was another area of high export production, on the order of 30 g C m^{-2} yr^{-1} (∼2.5 mol C m^{-2} yr^{-1}). Although none of the floats analyzed in this study reported data from the Patagonian shelf, NCP estimates from Zones T1-T3 were in relatively good agreement with Schlitzer's export production estimate from the Southern Ocean belt.

Johnson et al. (2017b) reported maximum annual NCP estimates of 3–4 mol C m^{-2} yr^{-1} between latitudes of ∼40°S and 60°S, with decreases to lower NCP both to the north (<1 mol C m^{-2} yr^{-1}) and south (∼2 mol C m^{-2} yr^{-1}). They collected data from several floats around the Southern Ocean, with only two (5902112 and 5904475) from the Argentine Basin study area. However, the latitudinal gradient and range of NCP estimates agree well with those reported in this study.

MacCready and Quay (2001) utilized a budget approach to evaluate NO_3^- uptake and remineralization across the Southern Ocean between 35°S and 80°S. They binned the data into 5° latitudinal bands as meridional gradients are expected to be much larger than zonal gradients. Ultimately, they found low annual carbon export ≤1 mol C m^{-2} yr^{-1} southward of 55°S, highest rates (3.6–4.0 mol C m^{-2} yr^{-1}) between 45°S and 55°S, a slightly lower rate of 2.1 mol C m^{-2} yr^{-1} between 40°S and 45°S, and a decrease to <1 mol C m^{-2} yr^{-1} north of 40°S. This northward decline in productivity (particularly the large decrease north of 40°S), like that reported by Johnson et al. (2017b), agrees relatively well with the results of this study.

4.5. Apparent Discrepancy Between NO_3^- Drawdown and Chla

Munro et al. (2015) noted that NCP rates estimated from their mixed layer phosphate (PO_4^{3-}) and DIC budgets in the Drake Passage were highest before mid-December, and daily NCP rates during austral summer months were comparatively low. They found that the higher NCP rates in spring resulted from nutrient drawdown within a deeper mixed layer that was resupplied with nutrients via episodic entrainment events. They also noted that the higher spring NCP rates disagreed with satellite-based estimates that implied ∼40% of NCP occurred during austral summer months.

The primary drawdown of NO_3^- observed in this study occurred between October and December across all five zones (Figures 5 and 6), in apparent agreement with the findings of Munro et al. (2015). However, while NO_3^- drawdown may have been completed by January in Zone T1, the highest chla concentrations were observed in January-March (Figure 5p), perhaps as a result of increased water column stratification, which would limit the vertical supply of nutrients, particularly iron, into the mixed layer (e.g., Lefevre & Watson, 1999).

Furthermore, although NO_3^- drawdown appeared to be relatively rapid in austral spring, chla concentrations persisted through both spring and summer within the mixed layer in Zones T2 (Figure 5q) and T3 (Figure 5r), and deeper in the water column in Zones T4 (Figure 5s) and T5 (Figure 5t), where the subsurface chla maximum ranged between 75 and 150 m. However, after winter convection, maximum chla concentrations were again observed within the mixed layer in austral spring until NO_3^- concentrations were drawn down to zero.

While NO_3^- concentrations exceeded 5 μmol kg^{-1} within the mixed layer in Zones T1-T3 throughout the year and NO_3^- drawdown appeared to be relatively restricted to austral spring, we suggest that the primary production implied by the persistent chla concentrations observed during austral summer may have been fueled by regenerated nitrogen sources, such as ammonium (NH_4^+) or urea, as opposed to new nitrogen (i.e., NO_3^-) (Eppley & Peterson, 1979) since low concentrations of iron can reduce rates of new production as several enzymes required for photosynthesis, nitrate assimilation, and nitrogen fixation are iron dependent (Brzezinski et al., 2003; Timmermans et al., 1994).

Brzezinski et al. (2003) suggested that low iron concentrations in the Pacific sector (along 170°W) of the Southern Ocean near the Polar Front (53°–63°S) resulted in a preference of phytoplankton on regenerated nitrogen sources over NO_3^- as assimilation of the former requires less iron and energy compared to NO_3^- assimilation. They found significant differences in silicon:carbon:nitrogen (Si:C:N) ratios in terms of gross versus net uptake, implying that, while gross uptake ratios were close to Redfield proportions, preferential remineralization of carbon and (especially) nitrogen resulted in larger net uptake and incorporation of silicic acid ($Si(OH)_4^-$) into the standing stock of particulate organic matter (presumably increasing the export of Si out of the euphotic zone). The relevant corollary to these findings is that new nitrogen (NO_3^-) made up a relatively small amount of the total nitrogen used to support photosynthesis, with regenerated nitrogen sources being the predominate supply. They further suggest low iron concentrations may be responsible for their observations as $Si(OH)_4^-$:NO_3^- uptake ratios are expected to be >> 1 in iron-depleted conditions. They argued that under low iron conditions, a decline in NO_3^- uptake can be balanced by increased utilization of urea and ammonium, both of which are less dependent upon iron for assimilation. In addition, Arrigo et al. (1999) also argued that diatoms in the Ross Sea were obtaining up to ~31% of their needed nitrogen supply from sources other than NO_3^-. They further argued that relatively low (<1) $Si(OH)_4^-$:NO_3^- uptake ratios may be explained by the utilization of recycled nitrogen instead of NO_3^- due to iron limitation.

As we do not have any measurements of iron, $Si(OH)_4^-$, or NH_4^+ concentrations from the floats, these arguments and suggestions remain speculation. However, numerous studies in the Southern Ocean have reported similar transitions from NO_3^- uptake in spring and early summer (when light, macronutrients, and micronutrients are abundant), followed by uptake primarily of regenerated nitrogen (e.g., NH_4^+) as iron and/or $Si(OH)_4^-$ concentrations decrease and the phytoplankton community composition shifts from larger-celled organisms (e.g., diatoms) to smaller-celled organisms that may thrive in conditions of lower light and iron availability and take advantage of higher NH_4^+ concentrations resulting from heterotrophic processing (e.g., zooplankton grazing) of the preceding spring bloom (Flynn et al., 2021; Lourey et al., 2003; Mdutyana et al., 2020; Smith et al., 2022; Stirnimann et al., 2021).

5. Conclusions

The existing distribution of core- and BGC-Argo floats was sufficient to separate the Argentine Basin into five hydrographic zones, based on potential temperature distributions at 100 m. Biogeochemical data were sufficient for estimating median monthly profiles of these zones that were then utilized to determine annual NCP from the seasonal drawdown of NO_3^-. The deployment of additional floats in this region will enhance the capability for future studies to examine additional scales of variability.

The position and alignment of the fronts separating the five zones explored in this study were similar, but not exact, between methods employing θ at 100 m (this work) and σ_θ at 450 m (Artana et al., 2018). Maps of θ and NO_3^- at 10 m, 100 m, 200 m, and 300 m exhibited similar positions and alignments of most fronts; however, our results suggest that the specific method used to define fronts can result in differences in NCP estimates within comparable zones of up to ~1 mol C m^{-2} yr^{-1}. The choice of integration depth and the specific method of calculation for estimating the seasonal drawdown had impacts of similar magnitude. Overall, NCP in the Argentine Basin exhibited highest values of 3–4 mol C m^{-2} yr^{-1} in the region south of 40°S, with values decreasing to <1 mol C m^{-2} yr^{-1} between 40°S and 25°S. These estimates were in good agreement with independent studies.

Is there an advantage to using fronts/zones versus latitudinal bands to estimate NCP? There is potential in using fronts to delineate regional estimates of NCP depending on the availability of data as latitude bands/zonal averaging may require coarser resolution (e.g., 5° bins; MacCready & Quay, 2001) to provide sufficient data for mapping seasonal or monthly timeseries. Furthermore, latitude bands may cross fronts in different months or seasons, or fail to take into account fronts that are not strictly meridional (e.g., see Figures 3b and 3d), introducing biases into the analyses. While one might expect such biases to be smoothed/averaged out assuming enough data are available, this may not always be the case. Additional work may be necessary to remove profiles that appear to cross fronts (e.g., Johnson et al., 2017b), limiting the available data set. In contrast, the definition of fronts/zones may be advantageous as θ and NO_3^- maps (see Figure S5 in Supporting Information S1) agree reasonably well in terms of the position and alignment of fronts. The separation of the data into zones prior to calculating monthly means/medians for seasonal NO_3^- drawdown calculations are therefore likely not to suffer from uncertainties due to horizontal advection across such fronts/boundaries.

The BGC-Argo float data exhibited large, meridional gradients in physical and biogeochemical properties at 100 and 450 m. At 100 m, the NO_3^- concentrations decreased from 30 to 35 μmol kg^{-1} at ~55°S to <10 μmol kg^{-1} at ~40°S, and again decreased rather abruptly north of 40°S to <2 μmol kg^{-1}. While northward transport of high nutrient waters from the south supply NO_3^- at multiple depths, the mean seasonal cycles shown for each zone indicates winter mixing to depths >100 m also serves to supply the euphotic zone with nutrients to support primary production in the spring and summer months; the impact of vertical mixing becomes especially more important north of 50°S (e.g., Zone T3) and the dominant supply process north of 40°S (e.g., Zones T4 and T5).

Concentrations of chla were relatively high during austral summer despite the majority of NO_3^- drawdown having been completed by December/January. One possible explanation for this apparent discrepancy is that primary production is fueled by regenerated sources of nitrogen during these months. This could also explain part of the apparent disconnect in the timing/duration of NCP based on geochemical budgets versus remote sensing as described in Munro et al. (2015).

This study shows the capability for using BGC-Argo floats to study biogeochemical cycles throughout the year in highly dynamic oceanic regions with multiple fronts. Additional deployments of floats equipped with biogeochemical sensors will enhance the capability of future studies to address additional variations on multiple temporal and spatial scales in the Argentine Basin and other regions throughout the global ocean.

Data Availability Statement

All data (Argo, 2023) used in this paper are freely available from the Argo Global Data Assembly Center (GDAC) at http://www.coriolis.eu.org/Data-Products.

Acknowledgments

Funding for Argo operations at the University of Washington is provided by the National Science Foundation, via BGC-Argo (1946578 and 2110258) and the Southern Ocean Carbon and Climate Observations and Modeling (SOCCOM) Project (PLR-1425989 and OPP-1936222), as well as the National Oceanic and Atmospheric Administration (NA20OAR4320271) and the National Aeronautics and Space Administration (NNX14AP49G). The Argo Program is part of the Global Ocean Observing System. We thank all of the personnel who have contributed to the construction of the profiling float array and data system, personnel who have assisted at sea in deployments, and the captains and crew of the vessels that have deployed these floats. We would also like to especially thank Tanya Maurer and Josh Plant, of the Monterey Bay Aquarium Research Institute, who process all of the biogeochemical data from the BGC-Argo floats used in this study. They were exceedingly helpful in answering questions about the data, formats, and processing steps. We would also like to thank the two reviewers of this manuscript as they provided invaluable comments and suggestions that greatly improved the quality and readability of this manuscript.

References

Alkire, M. B., D'Asaro, E., Lee, C., Perry, M. J., Gray, A., Cetinic, I., et al. (2012). Estimates of net community production and export using high-resolution, Lagrangian measurements of O_2, NO_3^-, and POC through the evolution of a spring diatom bloom in the North Atlantic. *Deep-Sea Research I*, *64*, 157–174. https://doi.org/10.1016/j.dsr.2012.01.012

Argo (2023). Argo float data and metadata from global data assembly Centre (Argo GDAC). [Dataset. SEANOE. https://doi.org/10.17882/42182#101760

Arrigo, K. R., Robinson, D. H., Worthen, D. L., Dunbar, R. B., DiTullio, G. R., VanWoert, M., & Lizotte, M. P. (1999). Phytoplankton community structure and the drawdown of nutrients and CO_2 in the Southern Ocean. *Science*, *283*(5400), 365–367. https://doi.org/10.1126/science.283.5400.365

Artana, C., Lellouche, J.-M., Park, Y.-H., Garric, G., Koenig, Z., Sennéchael, N., et al. (2018). Fronts of the Malvinas Current System: Surface and subsurface expressions revealed by satellite altimetry, Argo floats, and Mercator operational model outputs. *Journal of Geophysical Research*, *123*(8), 5261–5285. https://doi.org/10.1029/2018JC013887

Bittig, H. C., Steinhoff, T., Claustre, H., Fiedler, B., Williams, N. L., Sauzède, R., et al. (2018). An alternative to static climatologies: Robust estimation of open ocean CO2 variables and nutrient concentrations from T, S, and O_2 data using Bayesian neural networks. *Frontiers in Marine Science*, *5*, 328. https://doi.org/10.3389/fmars.2018.00328

Brzezinski, M. A., Dickson, M.-L., Nelson, D. M., & Sambrotto, R. (2003). Ratios of Si, C and N uptake by microplankton in the Southern Ocean. *Deep-Sea Research II*, *50*(3–4), 619–633. https://doi.org/10.1016/s0967-0645(02)00587-8

Carter, B. R., Feely, R. A., Williams, N. L., Dickson, A. G., Fong, M. B., & Takeshita, Y. (2018). Updated methods for global locally interpolated estimation of alkalinity, pH, and nitrate. *Limnology and Oceanography: Methods*, *16*(2), 119–131. https://doi.org/10.1002/lom3.10232

Dunne, J. P., Sarmiento, J. L., & Gnanadesikn, A. (2007). A synthesis of global particle export from the surface ocean and cycling through the ocean interior and on the seafloor. *Global Biogeochemical Cycles*, *21*(4). https://doi.org/10.1029/2006GB002907

Eppley, R. W., & Peterson, B. J. (1979). Particulate organic matter flux and planktonic new production in the deep ocean. *Nature*, *282*(5740), 677–680. https://doi.org/10.1038/282677a0

Flynn, R. F., Bornman, T. G., Burger, J. M., Smith, S., Spence, K. A. M., & Fawcett, S. E. (2021). Summertime productivity and carbon export potential in the Weddell Sea, with a focus on the waters adjacent to Larsen C Ice Shelf. *Biogeosciences*, *18*(22), 6031–6059. https://doi.org/10.5194/bg-18-6031-2021

Fontela, M., Velo, A., Gilcoto, M., & Pérez, F. F. (2021). Anthropogenic CO_2 and ocean acidification in Argentine Basin Water Masses over almost five decades of observations. *Science of the Total Environment*, *779*, 146570. https://doi.org/10.1016/j.scitotenv.2021.146570

Gordon, A. L. (1989). Brazil-Malvinas Confluence - 1984. *Deep-Sea Research I*, *36*(3), 359–384. https://doi.org/10.1016/0198-0149(89)90042-3

Hennon, T. D., Riser, S. C., & Mecking, S. (2016). Profiling float-based observations of net respiration beneath the mixed layer. *Global Biogeochemical Cycles*, *30*(6), 920–932. https://doi.org/10.1002/2016BG005380

Johnson, K. S., Coletti, L., Jannasch, H., Sakamoto, C., Swift, D., & Riser, S. (2013). Long-term nitrate measurements in the ocean using the in situ ultraviolet spectrophotometer: Sensor integration into the apex profiling float. *Journal of Atmospheric and Oceanic Technology*, *30*(8), 1854–1866. https://doi.org/10.1175/JTECH-D-12-00221.1

Johnson, K. S., Plant, J. N., Coletti, L. J., Jannasch, H. W., Sakamoto, C. M., Riser, S. C., et al. (2017a). Biogeochemical sensor performance in the SOCCOM profiling float array. *Journal of Geophysical Research: Oceans*, *122*(8), 6416–6436. https://doi.org/10.1002/2017JC012838

Johnson, K. S., Plant, J. N., Dunne, J. P., Talley, L. D., & Sarmiento, J. L. (2017b). Annual nitrate drawdown observed by SOCCOM profiling floats and the relationship to annual net community production. *Journal of Geophysical Research*, *122*(8), 6668–6683. https://doi.org/10.1002/2017JC012839

Jullion, L., Heywood, K. J., Naveira Garabato, A. C., & Stevens, D. P. (2010). Circulation and water mass modification in the Brazil-Malvinas Confluence. *Journal of Physical Oceanography*, *40*(5), 845–864. https://doi.org/10.1175/2009JPO4174.1

Lefevre, N., & Watson, A. J. (1999). Modeling the geochemical cycles of iron in the oceans and its impact on atmospheric CO2 concentrations. *Global Biogeochemical Cycles*, *13*(3), 727–736. https://doi.org/10.1029/1999gb900034

Lourey, M. J., Trull, T. W., & Sigman, D. M. (2003). Sensitivity of δ^{15}N of nitrate, surface suspended and deep sinking particulate nitrogen to seasonal nitrate depletion in the Southern Ocean. *Global Biogeochemical Cycles*, *17*(3), 1081. https://doi.org/10.1029/2002GB001973

Maamaatuaiahutapu, K., Garcon, V. C., Provost, C., Boulhadid, M., & Bianchi, A. A. (1994). Spring and winter water mass composition in the Brazil-Malvinas Confluence. *Journal of Marine Research*, *52*(3), 397–426. https://doi.org/10.1357/0022240943077064

MacCready, P., & Quay, P. (2001). Biological export flux in the Southern Ocean estimated from a climatological nitrate budget. *Deep-Sea Research II*, *48*(19–20), 4299–4322. https://doi.org/10.1016/s0967-0645(01)00090-x

Maurer, T. L., Plant, J. N., & Johnson, K. S. (2021). Delayed-mode quality control of oxygen, nitrate, and pH data on SOCCOM biogeochemical profiling floats. *Frontiers in Marine Science*, *8*. https://doi.org/10.3389/fmars.2021.683207

Mdutyana, M., Thomalla, S. J., Philibert, R., Ward, B. B., & Fawcett, S. E. (2020). The seasonal cycle of nitrogen uptake and nitrification in the Atlantic sector of the Southern Ocean. *Global Biogeochemical Cycles*, *34*(7), e2019GB006363. https://doi.org/10.1029/2019GB006363

Munro, D. R., Lovenduski, N. S., Stephens, B. B., Newberger, T., Arrigo, K. R., Takahashi, T., et al. (2015). Estimates of net community production in the Southern Ocean determined from time series observations (2002-2011) of nutrients, dissolved inorganic carbon, and surface ocean pCO_2 in Drake Passage. *Deep-Sea Research II*, *114*, 49–63. https://doi.org/10.1016/j.dsr2.2014.12.014

Orsi, A. H., Whitworth, T., & Nowlin, W. D. (1995). On the meridional extent and fronts of the Antarctic Circumpolar Current. *Deep-Sea Research I*, *42*(5), 641–673. https://doi.org/10.1016/0967-0637(95)00021-w

Peterson, R. G., & Whitworth, T., III. (1989). The Subantarctic and Polar Fronts in relation to deep water masses through the southwestern Atlantic. *Journal of Geophysical Research*, *94*(C8), 10817–10838. https://doi.org/10.1029/jc094ic08p10817

Plant, J. N., Johnson, K. S., Sakamoto, C. M., Jannasch, H. W., Coletti, L. J., Riser, S. C., & Swift, D. D. (2016). Net community production at Ocean Station Papa observed with nitrate and oxygen sensors on profiling floats. *Global Biogeochemical Cycles*, *30*(6), 859–879. https://doi.org/10.1002/2015GB005349

Provost, C., Gana, S., Garçon, V., Maamaatuaiahutapu, K., & England, M. (1995). Hydrographic conditions in the Brazil Malvinas Confluence during austral summer 1990. *Journal of Geophysical Research*, *100*(C6), 10655–10678. https://doi.org/10.1029/94jc02864

Roesler, C., Uitz, J., Claustre, H., Boss, E., Xing, X., Organelli, E., et al. (2017). Recommendations for obtaining unbiased chlorophyll estimates from in situ chlorophyll fluorometers: A global analysis of WET Labs ECO sensors. *Limnology and Oceanography: Methods*, *15*(6), 572–585. https://doi.org/10.1002/lom3.10185

Schlitzer, R. (2002). Carbon export fluxes in the Southern Ocean: Results from inverse modeling and comparison with satellite-based estimates. *Deep-Sea Research II*, *49*(9–10), 1623–1644. https://doi.org/10.1016/s0967-0645(02)00004-8

Schlitzer, R. (2014). Ocean data view, version 4.6.3 (64-bit) [Software]. https://odv.awi.de

Siegel, D. A., Buesseler, K. O., Doney, S. C., Sailley, S. F., Behrenfeld, M. J., & Boyd, P. W. (2014). Global assessment of ocean carbon export by combining satellite observations and food-web models. *Global Biogeochemical Cycles*, *28*(3), 181–196. https://doi.org/10.1002/2013GB004743

Smith, S., Altieri, K. E., Mdutyana, M., Walker, D. R., Parntt, R. G., Gallie, S., et al. (2022). Biogeochemical controls on ammonium accumulation in the surface layer of the Southern Ocean. *Biogeosciences*, *19*(3), 715–741. https://doi.org/10.5194/bg-19-715-2022

Stephenson, G. R., Jr., Gille, S. T., & Sprintall, J. (2012). Seasonal variability of upper ocean heat content in Drake Passage. *Journal of Geophysical Research*, *117*(C4), C04019. https://doi.org/10.1029/2011JC007772

Stirnimann, L., Bornman, T. G., Verheye, H. M., Bachèlery, M.-L., van der Poel, J., & Fawcett, S. E. (2021). Plankton community composition and productivity near the Subantarctic Prince Edward Islands archipelago in autumn. *Limnology and Oceanography*, *66*(12), 4140–4158. https://doi.org/10.1002/lno.11949

Timmermans, K. R., Stolte, W., & de Baar, H. J. W. (1994). Iron-mediated effects on nitrate reductase in marine phytoplankton. *Marine Biology*, *121*(2), 389–396. https://doi.org/10.1007/bf00346749

Volkov, D. L., & Fu, L.-L. (2008). The role of vorticity fluxes in the dynamics of the Zapiola Anitcyclone. *Journal of Geophysical Research*, *113*(C11015), C11015. https://doi.org/10.1029/2008JC004841

Wong, A., Keeley, R., & Carval, T., & the Argo Data Management Team. (2022). Argo Quality Control Manual for CTD and Trajectory Data. https://doi.org/10.13155/33951

Wong, A. P. S., Johnson, G. C., & Owens, W. B. (2003). Delayed-mode calibration of autonomous CTD profiling float salinity data by θ-S climatology. *Journal of Atmospheric and Oceanic Technology*, *20*(2), 308–318. https://doi.org/10.1175/1520-0426(2003)020<0308:dmcoac>2.0.co;2

Wong, A. P. S., Wijffels, S. E., Riser, S. C., Pouliquen, S., Hosoda, S., Roemmich, D., et al. (2020). Argo data 1999–2019: Two million temperature-salinity profiles and subsurface velocity observations from a global array of profiling floats. *Frontiers in Marine Science*, *7*. https://doi.org/10.3389/fmars.2020.00700

Xing, X., Claustre, H., Blain, S., D'Ortenzio, F., Antoine, D., Ras, J., & Guinet, C. (2012). Quenching correction for in vivo chlorophyll fluorescence acquired by autonomous platforms: A case study with instrumented elephant seals in the Kerguelen region (Southern Ocean). *Limnology and Oceanography: Methods*, *10*(7), 483–495. https://doi.org/10.4319/lom.2012.10.483